



# Bifunctionally active and durable hierarchically porous transition metal-based hybrid electrocatalyst for rechargeable metal-air batteries

Min Ho Seo<sup>a,b,1</sup>, Moon Gyu Park<sup>a,1</sup>, Dong Un Lee<sup>a</sup>, Xiaolei Wang<sup>a</sup>, Wook Ahn<sup>a</sup>, Seung Hyo Noh<sup>c</sup>, Sung Mook Choi<sup>d</sup>, Zachary P. Cano<sup>a</sup>, Byungchan Han<sup>c</sup>, Zhongwei Chen<sup>a,\*</sup>

<sup>a</sup> Department of Chemical Engineering, Waterloo Institute for Nanotechnology, Waterloo Institute of Sustainable Energy, University of Waterloo, 200 University Ave. W, Waterloo, ON, N2L 3G1, Canada

<sup>b</sup> Hydrogen & Fuel Cell Center, New & Renewable Energy Research Division, Korea Institute of Energy Research (KIER) 20-41, Sinjaesaengeneogi-ro, Haseo-myeon, Buan-gun, Jeollabuk-do, 56332, South Korea

<sup>c</sup> Department of Chemical and Biomolecular Engineering, Yonsei University, Seoul, 120-749, South Korea

<sup>d</sup> Surface Technology Division, Korea Institute of Materials Science (KIMS), Changwon, 641-010, South Korea

## ARTICLE INFO

### Keywords:

Rechargeable metal-air battery  
3-dimensionally ordered mesoporous structure  
Oxygen electrocatalytic reactions  
Bifunctional electrocatalysts  
Density functional theory

## ABSTRACT

In this work, we show an effective strategy combining experimental and computational methods to explore and clarify rational design approaches utilizing transition metals for enhanced electrocatalysis of oxygen reactions. We report a bifunctional electrocatalyst synthesized by a chemical deposition of palladium (Pd) nanoparticles on three-dimensionally ordered mesoporous cobalt oxide (Pd@3DOM-Co<sub>3</sub>O<sub>4</sub>) demonstrating extreme stability and activity towards electrocatalytic oxygen reduction and evolution reactions (ORR and OER). Pd@3DOM-Co<sub>3</sub>O<sub>4</sub> exhibits a significantly positive-shifted ORR half-wave potential of 0.88 V (vs. RHE) and a higher OER current density of 41.3 mA cm<sup>-2</sup> measured at 2.0 V (vs. RHE) relative to non-deposited 3DOM-Co<sub>3</sub>O<sub>4</sub>. Moreover, in terms of durability, Pd@3DOM-Co<sub>3</sub>O<sub>4</sub> demonstrates a negligible half-wave potential loss with 99.5% retention during ORR and a high current density retention of 96.4% during OER after 1000 cycles of accelerated degradation testing (ADT). *Ab-initio* computational simulation of the oxygen reactions reveals that the modification of the electronic structure by combining Pd and Co<sub>3</sub>O<sub>4</sub> lowers the Pd d-band center and enhances the electron abundance at the Fermi level, resulting in improved kinetics and conductivity. Furthermore, it is elucidated that the enhanced electrochemical stability is attributed to an elevated carbon corrosion potential ( $U_{\text{corr,C}}$ ) for the Pd@3DOM-Co<sub>3</sub>O<sub>4</sub> surface and an increased dissolution potential ( $U_{\text{diss}}$ ) of Pd nanoparticles. Meanwhile, synergistic improvements in the bifunctional activity resulting from the combination of Pd and 3DOM-Co<sub>3</sub>O<sub>4</sub> were confirmed by both electrochemical and physical characterization methods, which highlights the practical viability of Pd@3DOM-Co<sub>3</sub>O<sub>4</sub> as an efficient bifunctional catalyst for rechargeable metal-air batteries.

## 1. Introduction

Increased awareness of the harmful effects of fossil fuel use, and accompanying greenhouse gas emissions causing global climate change, have led to a rigorous push for the development of sustainable energy conversion and storage systems [1,2]. There has been tremendous interest in pursuing both fundamental and applied research towards developing new types of sustainable energy systems such as fuel cells and metal-air batteries [2,3], which are expected to have positive impacts on the commercialization of smart-grid energy storage and electrified vehicles in the near future [4]. In particular, metal-air batteries boasting extremely high volumetric and gravimetric energy densities

have recently been in the spotlight of energy research for further development of advanced energy storage applications [3,5,6]. However, the current metal-air battery systems have a few critical challenges, including i) large overpotentials resulting from sluggish oxygen reduction reaction (ORR) and oxygen evolution reaction (OER) kinetics and ii) catalyst degradation due to relatively unstable electrochemistry during repetitive discharge and charge cycles. These challenges arise from insufficient activity and durability of the air electrode, one of the main components of a metal-air battery, which includes electrocatalysts that lower activation energies of the reactions to reduce overpotential associated with discharge and charge processes [7]. Hence, recent research efforts in energy materials development have focused on

\* Corresponding author.

E-mail address: [zhwchen@uwaterloo.ca](mailto:zhwchen@uwaterloo.ca) (Z. Chen).

<sup>1</sup> These authors contributed equally to this work.

addressing the above challenges, which would ultimately enable commercialization of electrically rechargeable metal-air batteries [8–18].

Recent approaches combining density functional theory (DFT) and *ab-initio* studies with experimental studies have allowed researchers to precisely simulate catalytic activities and gain fundamental understandings of the oxygen reactions [19,20]. Further, they have enabled the development of sufficiently active low-cost catalysts by allowing not only the design of efficient non-precious material-based catalysts, but also the effective minimization of noble metal loadings in noble metal-based catalysts. Some examples of these oxygen reaction catalysts include non-precious transition metal-based materials ( $\text{Mn}_x\text{O}_y$ ,  $\text{Co}_x\text{O}_y$ ,  $\text{NiCo}_x\text{O}_y$ ,  $\text{LaNi}_x\text{O}_y$ , etc.) [14–18,21,22], functionalized carbon-based materials (heteroatom-doped graphene and carbon nanotubes, etc.) [10–12,23], metal–nitrogen complexes ( $\text{M-N}_x/\text{C}$ ) [24–26], and noble metal-based materials ( $\text{Pt}_3\text{Ni}$ ,  $\text{Pt}_3\text{Co}$ ,  $\text{Pt}_3\text{Y}$ , etc.) [27,28].

As one of the most notable examples,  $\text{Pt}_3\text{Ni}$  was revealed by Nørskov and associates to show enhanced ORR activity relative to Pt due to a downward shifted d-band center in its electronic structure, which results in weaker adsorption with oxygen intermediates on the catalytic surface [27,29–35]. For non-precious catalysts such as metal–nitrogen complexes and metal oxides, understanding the  $e_g$  orbital of valence electrons makes it possible to predict the oxygen reactivity, which can be controlled by the number of outer electrons of transition metals [17,36–38]. The electrochemical stability during the oxygen reduction and evolution reactions has been associated with the dissolution potential and cohesive energy term, which can be modified by changing morphology and size of the transition metal nanoparticles as well as the supporting materials [39–42]. However, most reports incorporating the above design strategy have focused solely on catalytic activities without also considering long-term durability.

Regarding the stability of rechargeable metal-air batteries, thermodynamic electrochemical durability of cathode materials is extremely restricted due to their instability during the charging process, which typically occurs at high potentials (over 0.4 V vs SHE). This potential range is comparable to the ORR potential region of fuel cell systems using acidic media; these harsh conditions can dissolve metal and carbon-based catalysts, resulting in severe degradation of their electrochemical performance. Although metal oxides are generally more able to retain their solid phase during metal-air battery charging, they are usually not solely used because of their poor conductivity due to band gaps in their electronic structure. Therefore, carbon materials are typically required as conductive and dispersive additives within the electrode, inevitably leading to inherent thermodynamic instability due to  $\text{CO}_2$  oxidation above 0.207 V vs. RHE.

To address this challenge, a highly efficient and durable bifunctional oxygen electrocatalyst was designed by combining three-dimensionally ordered mesoporous spinel cobalt oxide ( $3\text{DOM-Co}_3\text{O}_4$ ) with palladium (Pd) nanoparticle deposition. Morphological advantages of the 3DOM structure of  $\text{Co}_3\text{O}_4$  facilitating diffusion of oxygen molecules in and out of the structure can lead to reduced overpotentials for the ORR and OER. Pd was introduced into the 3DOM  $\text{Co}_3\text{O}_4$  by expecting synergistic effects, especially to take full advantage of its significant stability as solid phase below 0.810 V vs. SHE (Standard Hydrogen Electrode) by the Nernst equation with using  $10^{-6}$  M of  $\text{Pd}^{2+}(\text{aq})$  at pH = 0, as well as the well-known excellent electrocatalytic ORR activity. Resulting from our systematic prediction, we demonstrated synergistically enhanced bifunctional activity and durability within the operating conditions of electrically rechargeable metal-air batteries. In addition, the catalyst was modelled with DFT-based *ab-initio* analysis to elucidate the underlying catalytic mechanisms and interpret the carbon oxidation potentials ( $U_{\text{corr,C}}$ ) on the surface of the various catalysts, as well as the dissolution potential ( $U_{\text{diss}}$ ) of various Pd species on the catalyst surface to validate its remarkably high durability. Overall, this investigation provides a framework for rationally designing bifunctional catalysts based on the thermodynamic principles that govern electrochemical stabilities for corrosion-resistant

electrocatalysis, and demonstrates the application of the developed catalyst in a single-cell rechargeable zinc-air battery to highlight its performance and durability.

## 2. Material and methods

### 2.1. Synthesis of $3\text{DOM-Co}_3\text{O}_4$ and $\text{Pd}@3\text{DOM-Co}_3\text{O}_4$

Three-dimensionally ordered mesoporous spinel cobalt oxide ( $3\text{DOM-Co}_3\text{O}_4$ ) was prepared by a facile sacrificing template method. First, polystyrene (PS) beads were synthesized by a simple polymerization employing styrene monomer, potassium persulfate ( $\text{K}_2\text{S}_2\text{O}_8$ ), and polyvinylpyrrolidone (PVP) all bought from Sigma-Aldrich Canada. 2.5 g of PVP was dissolved in 200 mL of distilled de-ionized (DDI) water heated to 70 °C. Next, the styrene monomer (24 mL) was added into the mixture and a certain volume of  $\text{K}_2\text{S}_2\text{O}_8$  dissolved DDI water ( $5 \text{ g L}^{-1}$ ) was slowly poured into the solution. The polymerization process was carried out for 24 h under vigorous stirring with a condenser used for preventing evaporation of the solution. Additionally,  $\text{N}_2$  gas continuously was purged into the flask to keep oxygen absent from the environment. The resultant PS solution was centrifuged at a low rate for more than 12 h to obtain a well-layered PS mass followed by a drying process at 60 °C. The well-layered PS beads were employed as a template material in this method, where the spherical PS beads conform to a three-dimensionally ordered hierarchically porous  $\text{Co}_3\text{O}_4$  structure with regularly connected voids. In a specific synthesis of  $3\text{DOM-Co}_3\text{O}_4$ , the PS beads were soaked for 4 h in a precursor solution of cobalt nitrate hexahydrate (30 mmol), citric acid (30 mmol) and ethanol (20 mL), allowing the solution to completely fill its voids. After drying at an ambient temperature for 24 h, the materials were heat-treated at 300 °C in an air stream (ramp rate of  $1^\circ\text{C min}^{-1}$ ) for 3 h to simultaneously melt the PS beads and solidify the cobalt precursor into the 3DOM structure. The annealed product was placed in a mixture of acetone and hexane (volume ratio of 1:1) at 60 °C for 30 min to dissolve the remaining PS, followed by drying at 80 °C for 4 h. The dried material was calcined in an air stream at 400 °C (ramp rate of  $1^\circ\text{C min}^{-1}$ ) for 3 h to obtain the spinel cobalt oxide crystal structure with a robust 3DOM framework ( $3\text{DOM-Co}_3\text{O}_4$ ). Next, Pd-deposited  $3\text{DOM-Co}_3\text{O}_4$  was synthesized by a facile reduction process. As-prepared  $3\text{DOM-Co}_3\text{O}_4$  (72 mg) was added into a round-bottom flask (50 mL) with Pd precursor solution in which the 30 mg  $\text{PdCl}_2$  (weight percent of Pd to  $\text{Co}_3\text{O}_4$  of 20%) was dissolved in a mixture of ethanol and hydrochloric acid with a volume ratio of 12:1. The mixture was gently stirred with a magnetic bar and refluxed for 6 h with addition of 10 mL ethylene glycol solution, followed by filtration and washing with ultrapure water. Finally, the obtained composite was dried at 80 °C under vacuum condition. As a reference, 20 wt.% Pd/C was also synthesized by the same method where activated carbon black was used instead of  $3\text{DOM-Co}_3\text{O}_4$  as the support.

### 2.2. Materials characterization

A variety of characterization techniques were selected for physico-chemical analysis of all the studied catalysts. Transmission electron microscopy (TEM) (JEOL 2010 F) and scanning electron microscopy (SEM) (LEO FESEM 1530) were used to investigate the morphology and structure of the catalysts. High-resolution TEM (HR-TEM), selected area electron diffraction (SAED), scanning transmission electron microscopy (STEM) and elemental mapping based on energy-dispersive X-ray spectroscopy (EDX) were utilized to identify the existence of Pd nanoparticles with  $3\text{DOM-Co}_3\text{O}_4$  as a supporting framework and to study the porosity, composition, and crystallinity of the composite. X-ray diffraction (XRD) (Bruker AXS D8 Advance) and X-ray photoelectron spectroscopy (XPS) (Thermal Scientific K-Alpha XPS spectrometer) were employed to characterize the crystal structure, elemental composition and the surface chemistry of the catalyst.

## 2.3. Electrochemical characterizations

### 2.3.1. Half-cell with RDE

A traditional three-electrode configuration, consisting of a glassy carbon (GC) electrode, platinum wire, and saturated calomel electrode (SCE) as the working electrode, counter electrode and reference electrode, respectively, was utilized to evaluate the electrochemical performance of the catalysts at room temperature. The electrocatalytic activities for ORR and OER were measured by a rotating disc electrode (RDE) half-cell technique and cyclic voltammetry (CV), where a CHI Electrochemical Station (Model 760D) was used to evaluate the performances. The tests were performed from 0 to  $-1.0$  V vs. SCE at 1600 rpm for ORR and from 0 to  $1.0$  V vs. SCE at 1600 rpm for OER. The scan rate for both electrochemical tests was  $10 \text{ mV s}^{-1}$ . The accelerated degradation testing (ADT) was conducted by performing CV ( $\sim 1000$  cycles) in the OER potential region of  $1\text{--}2$  V vs. RHE with a scan rate of  $50 \text{ mV s}^{-1}$ . The potential versus SCE was converted to potential versus RHE at room temperature according to  $E_{\text{RHE}} = E_{\text{SCE}} + 0.241 + 0.0591 \text{ pH}$ . The electrolyte was purged with pure oxygen and nitrogen gas for 30 min before ORR and OER measurements, respectively. The ORR polarization curves in oxygen-saturated electrolyte were corrected by subtracting background curves, which were obtained in nitrogen-saturated electrolyte, to eliminate capacitive currents during the ORR tests. All measurements were conducted in a  $0.1 \text{ M KOH}$  solution. The measured overpotentials ( $\eta$ ) for ORR and OER were based on the standard oxygen reduction potential ( $E^\circ = 1.23 \text{ V}$  vs. RHE), where  $\eta_{\text{ORR}} = 1.23 \text{ V} - \text{measured ORR potential (vs. RHE)}$  and  $\eta_{\text{OER}} = \text{measured OER potential (vs. RHE)} - 1.23 \text{ V}$ . Before testing, the GC electrode (diameter:  $5 \text{ mm}$ ) was polished using alumina suspension (particle size:  $0.05 \mu\text{m}$ ) on a smooth polishing cloth. The catalyst ink was prepared by mixing  $4 \text{ mg}$  of the catalyst and Vulcan Carbon (XC-72) (mass ratio of  $1:1$ ) in  $1 \text{ mL}$  of isopropanol (IPA) pre-treated by Nafion solution ( $0.3 \text{ wt.}\%$ ) followed by ultrasonication for  $30 \text{ min}$  to obtain a homogeneous ink.  $20 \mu\text{L}$  of the as-prepared ink was dropped with a micropipette onto the GC surface and dried under ambient conditions, leading to a catalyst loading of  $0.2 \text{ mg cm}^{-2}_{\text{catalyst}}$ . Precious metal catalysts consisting of platinum carbon (Pt/C,  $28.8 \text{ wt.}\%$  Pt), iridium carbon (Ir/C,  $20 \text{ wt.}\%$  Ir) and palladium carbon (Pd/C,  $20 \text{ wt.}\%$  Pd) were used as reference materials (without blending with Vulcan Carbon) to demonstrate the relative catalytic efficiency and practicality of bifunctionally active and stable Pd@3DOM- $\text{Co}_3\text{O}_4$ .

### 2.3.2. Rechargeable Zn-Air single cell

An air electrode was prepared by spray-coating the catalyst ink solution onto a gas diffusion layer (Ion Power Inc., SGL Carbon 35 BCE) with an air brush onto an active area of  $0.785 \text{ cm}^2$  (catalyst loading:  $1 \text{ mg cm}^{-2}$ ). The catalyst ink was prepared by mixing the catalyst and Vulcan Carbon in Nafion-containing ( $5 \text{ wt.}\%$ ) isopropanol (IPA) with a weight ratio of  $1:1$ , followed by ultrasonication for  $1 \text{ h}$  to obtain a homogeneously dispersed ink solution. Similarly to the half-cell evaluations, the commercial carbon-supported precious metal catalysts (Pt/C and Ir/C) were used to prepare reference air electrodes by the same method (without Vulcan Carbon). A zinc plate (OnlineMetals, Zinc Sheet EN 988), a microporous polypropylene membrane (Celgard 5550) and a  $6.0 \text{ M KOH}$  solution with  $0.2 \text{ M}$  zinc acetate were employed as the anode, separator and electrolyte, respectively. Stainless steel meshes were utilized as current collectors for the both anode and cathode sides. Galvanodynamic discharge and charge experiments were carried out with a multichannel potentiostat (Princeton Applied Research, VersaSTAT MC). With a wide range of currents (current density:  $0$  to  $\sim 60 \text{ mA cm}^{-2}$ ), discharge and charge profiles were obtained. Zn-air single cell cycling tests were operated by a cycling tester (BTSDA). The cycling was performed with  $10 \text{ min}$  cycles ( $5 \text{ min}$  discharge and  $5 \text{ min}$  charge) and a high current density of  $10 \text{ mA cm}^{-2}$ . Long term cycling tests were also conducted, where one cycle was  $10 \text{ h}$  ( $5 \text{ h}$  each for discharge and charge) at a relatively low current density ( $1 \text{ mA cm}^{-2}$ ).

## 2.4. Computational modeling and design

Density functional theory (DFT) calculations implemented in the Vienna ab initio simulation package (VASP) program were utilized for the present study [19,20,43]. Exchange-correlation energies of electrons were described by the Perdew, Burke and Ernzerhof (PBE) functional for generalized gradient approximation (GGA) [44,45]. Core electrons were replaced by the projector augmented wave (PAW) pseudo-potentials [46,47], and Kohn-Sham wave functions of valence electrons were expanded by the plane wave basis set with a cut-off energy of  $520 \text{ eV}$ . The Hubbard  $U$  parameter (GGA +  $U$ ) was employed to improve the description of correlation effects and to reduce the self-interaction error in bulk  $\text{Co}_3\text{O}_4$  [48–50]. The optimized effective interaction parameter  $U_{\text{eff}}$  ( $U_{\text{eff}} = U - J$ ) of  $3.4 \text{ eV}$  was used for Co ions in the  $\text{Co}_3\text{O}_4$  structure. All ions were fully relaxed during the structural optimization until the total energy was converged within  $10^{-4} \text{ eV}$ . A gamma point mesh with  $(15 \times 15 \times 15)$  k-points was used for the  $\text{Co}_3\text{O}_4$  ( $1 \times 1$ ) unit cell to sample the Brillouin zone for bulk calculation. Periodic boundary conditions were imposed on these unit cells in terms of the (001) surface direction, and a vacuum space of  $20 \text{ \AA}$  was employed to avoid interactions between the top and bottom surface. The first five layers were fixed from the bottom and the rest of the layers were relaxed. To calculate the total energies of  $\text{Co}_3\text{O}_4$  slab models on the (001) surface direction, a gamma point mesh of  $(5 \times 5 \times 1)$  and the Methfessel-Paxton smearing method were utilized [51]. On the relaxed  $\text{Co}_3\text{O}_4$  slab model, Pd ( $3 \times 2\sqrt{3}$ ) and carbon monolayers ( $4 \times 2\sqrt{3}$ ) were deposited on the (001)  $\text{Co}_3\text{O}_4$  surface. For the density of states (DOS) calculations, the tetrahedron method with Blöchl's corrections was employed [52]. From the projected density of states (p-DOS) of a Pd atom, d-band center values of Pd on the  $\text{Co}_3\text{O}_4$  surface are estimated using Eq. (1) [53]:

$$\varepsilon_d = \frac{\int_{-\infty}^{E_F} E p_d(E) dE}{\int_{-\infty}^{E_F} p_d(E) dE} \quad (1)$$

Here,  $\varepsilon_d$  is d-band center weight and  $p_d$  is the projected density of states onto the d band of a Pd atom.

## 3. Results and discussion

The schematic synthesis in Fig. 1 shows the facile synthesis procedure used to prepare Pd@3DOM- $\text{Co}_3\text{O}_4$ . 3DOM- $\text{Co}_3\text{O}_4$  was prepared by the template-assisted method using spherical PS beads, resulting in the structure shown in Fig. 2a. Chemical deposition of Pd was conducted on the surface of 3DOM- $\text{Co}_3\text{O}_4$  to obtain the final material, Pd@3DOM- $\text{Co}_3\text{O}_4$ . As shown in Fig. 2b, the 3DOM structure is clearly observed, which was maintained after the deposition of Pd by the reflux method. In addition to the TEM analysis, SEM characterization was conducted to verify the overall 3D morphologies of 3DOM  $\text{Co}_3\text{O}_4$  after the deposition of Pd. The 3DOM structure is clearly observed to be uniform over a large area, highlighting the robust synthesis technique and the resulting high surface area available for ORR and OER to occur. Detailed HR-TEM inspection of the pristine 3DOM- $\text{Co}_3\text{O}_4$  surface shown in Fig. 2a-1 reveals the typical (001) BCC surface of  $\text{Co}_3\text{O}_4$ , while the surface particles shown in Fig. 2b-1 display the (111) FCC face of Pd, confirmed by fast Fourier transform (FFT) diffraction. The elemental mapping of 3DOM- $\text{Co}_3\text{O}_4$  before Pd deposition shown in Fig. 2a-2 reveals Co and O distributed throughout the 3DOM backbone. The elemental mapping of Pd@3DOM- $\text{Co}_3\text{O}_4$ , on the other hand, reveals a mostly uniform distribution of Pd (with a few regions with higher concentration) in addition to Co and O as presented in Fig. 2b-2.

Additionally, the XRD pattern of Pd@3DOM- $\text{Co}_3\text{O}_4$  (Fig. 2a) shows typical peaks representative of both FCC Pd and BCC  $\text{Co}_3\text{O}_4$ , as observed in the TEM images before and after Pd deposition. The XRD patterns of Pd@3DOM- $\text{Co}_3\text{O}_4$  and 3DOM- $\text{Co}_3\text{O}_4$  (Fig. 2c-1 and c-2) are consistent with those of bulk Pd and  $\text{Co}_3\text{O}_4$  (Fig. 2c-3 and c-4) obtained

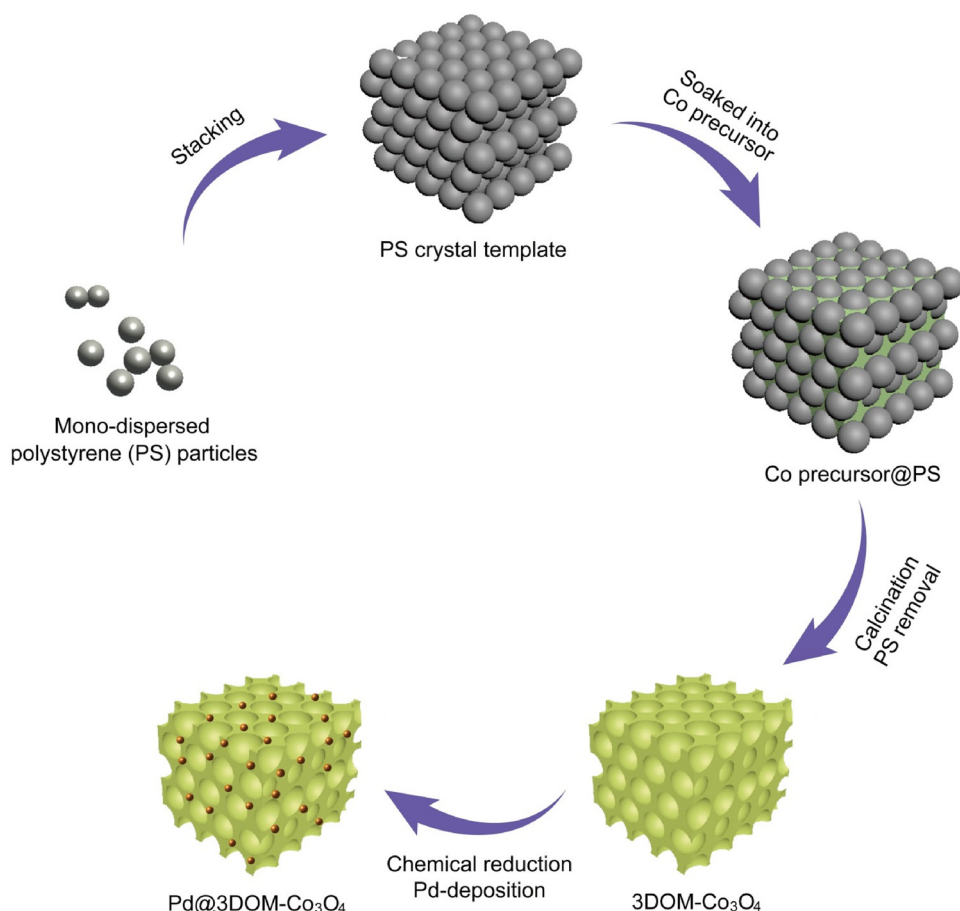


Fig. 1. Schematic synthesis of Pd-deposited 3D ordered mesoporous spinel cobalt oxide (Pd@3DOM-Co<sub>3</sub>O<sub>4</sub>).

from ICSD #64,915 and #24210, respectively, confirming successful formation of the Pd@3DOM-Co<sub>3</sub>O<sub>4</sub> composite. The hierarchically porous morphology of Pd@3DOM-Co<sub>3</sub>O<sub>4</sub> gives rise to a high specific surface area, which increases the active site exposure for the oxygen reactions. To confirm this, the N<sub>2</sub> adsorption-desorption isotherm of Pd@3DOM-Co<sub>3</sub>O<sub>4</sub> was obtained (Fig. 2d), which showed a typical type IV isotherm with a type II contribution and a clear H3 hysteresis loop in the higher relative pressure (P/P<sub>0</sub>) range of 0.45–1.0, which are characteristics of a mesoporous structure. The BET measurement revealed a specific surface area of 48.1 m<sup>2</sup> g<sup>−1</sup> and the BJH adsorption pore distribution result (Inset Fig. 2d) indicated the existence of mesopores with a dominant pore diameter of 170 nm, consistent with pore sizes observed in the micrographs above. The 3DOM structure is particularly beneficial in terms of facilitating the diffusion of gaseous oxygen and liquid electrolyte as well as improving the active material utilization, resulting in an overall electrochemical performance enhancement.

To further elucidate the electronic structures and surface elemental composition of the prepared 3DOM-Co<sub>3</sub>O<sub>4</sub> and Pd@3DOM-Co<sub>3</sub>O<sub>4</sub> materials, X-ray photoelectron spectroscopy (XPS) was conducted. As expected, the full XPS survey scan (Fig. 3a) of Pd@3DOM-Co<sub>3</sub>O<sub>4</sub> (red line) clearly revealed the existence of Co, Pd and O, while 3DOM-Co<sub>3</sub>O<sub>4</sub> (blue line) showed only Co and O. Moreover, the high resolution Pd 3d and Co 2p spectra of Pd@3DOM-Co<sub>3</sub>O<sub>4</sub> (Fig. 3b and c) and 3DOM-Co<sub>3</sub>O<sub>4</sub> (Fig. 3d) were de-convoluted to investigate the relationship between the electronic structures and surface elemental composition of the catalysts and their effects on electrocatalytic performances. In the d-band center theory, the electronic structure of the surface metal and its catalytic activity is correlated, and the core-level binding energy shift of a metal is an indicator for changes in the center of the occupied d-states [54,55]. The binding energy (BE) of the major spin–orbit split doublet

(Pd 3d<sub>5/2</sub> and Pd 3d<sub>3/2</sub>) for Pd@3DOM-Co<sub>3</sub>O<sub>4</sub> (Fig. 3b) appeared at approximately 335.46 and 340.78 eV (red lines), respectively, which are attributed to the presence of metallic Pd (Pd<sup>0</sup>). Another doublet, with BEs for Pd 3d<sub>5/2</sub> and 3d<sub>3/2</sub> peaks at approximately 336.56 and 341.96 eV (blue lines) are attributed to a higher oxidation state similar to that of PdO (Pd<sup>2+</sup>). The peak positions of metallic Pd are shifted to higher BE as the d-d orbital hybridization increases between Pd and Co<sub>3</sub>O<sub>4</sub>, compared with the core level BE (e.g., 335.3 eV for Pd 3d<sub>5/2</sub>) of Pd nanoparticles supported on carbon as shown in our previous study [55]. This indicates that the d-band center value of Pd on 3DOM-Co<sub>3</sub>O<sub>4</sub> is downward shifted compared to that of pure Pd, suggesting the potential to demonstrate a higher ORR activity. In the case of Co 2p in Pd@3DOM-Co<sub>3</sub>O<sub>4</sub> and 3DOM-Co<sub>3</sub>O<sub>4</sub> (Fig. 3c and 3d, respectively), the mixed valences of Co<sup>3+</sup>/Co<sup>2+</sup> were evaluated. The mixed valences of coexisting cobalt cations facilitate electron transfer by donor-acceptor chemisorption for reversible oxygen adsorption and desorption in the cubic spinel structure [55,56]. The BEs of Co<sup>3+</sup> (Co 2p<sub>3/2</sub> and Co 2p<sub>1/2</sub>) were observed at 780.86 and 796.06 eV (red lines in Fig. 3c) for Pd@3DOM-Co<sub>3</sub>O<sub>4</sub>, and 779.52 and 794.72 eV (red lines in Fig. 3d) for Co<sub>3</sub>O<sub>4</sub>, respectively. In Pd@3DOM-Co<sub>3</sub>O<sub>4</sub>, the Co<sup>3+</sup>/Co<sup>2+</sup> ratio was relatively higher than in Co<sub>3</sub>O<sub>4</sub> indicating that some Co<sup>2+</sup> was oxidized to Co<sup>3+</sup> after Pd deposition. This led to electron transfer from Co<sub>3</sub>O<sub>4</sub> to metallic Pd, resulting in a downward shift of the d-band center of Pd on 3DOM-Co<sub>3</sub>O<sub>4</sub>, which enhances the ORR activity. Regarding OER activity of Co<sub>3</sub>O<sub>4</sub>, there is a debate about whether Co<sup>2+</sup> or Co<sup>3+</sup> is the active site. Among recently reported studies, Wang et al. demonstrated Co<sup>2+</sup> is the active site using a series of in operando techniques [57], whereas P. W. Menezes et al. have claimed Co<sup>2+</sup> is catalytically inactive citing several reports [58,59]. Likewise, Siwen et al. have demonstrated Co<sup>3+</sup> is more catalytically active than Co<sup>2+</sup> for OER by synthesizing



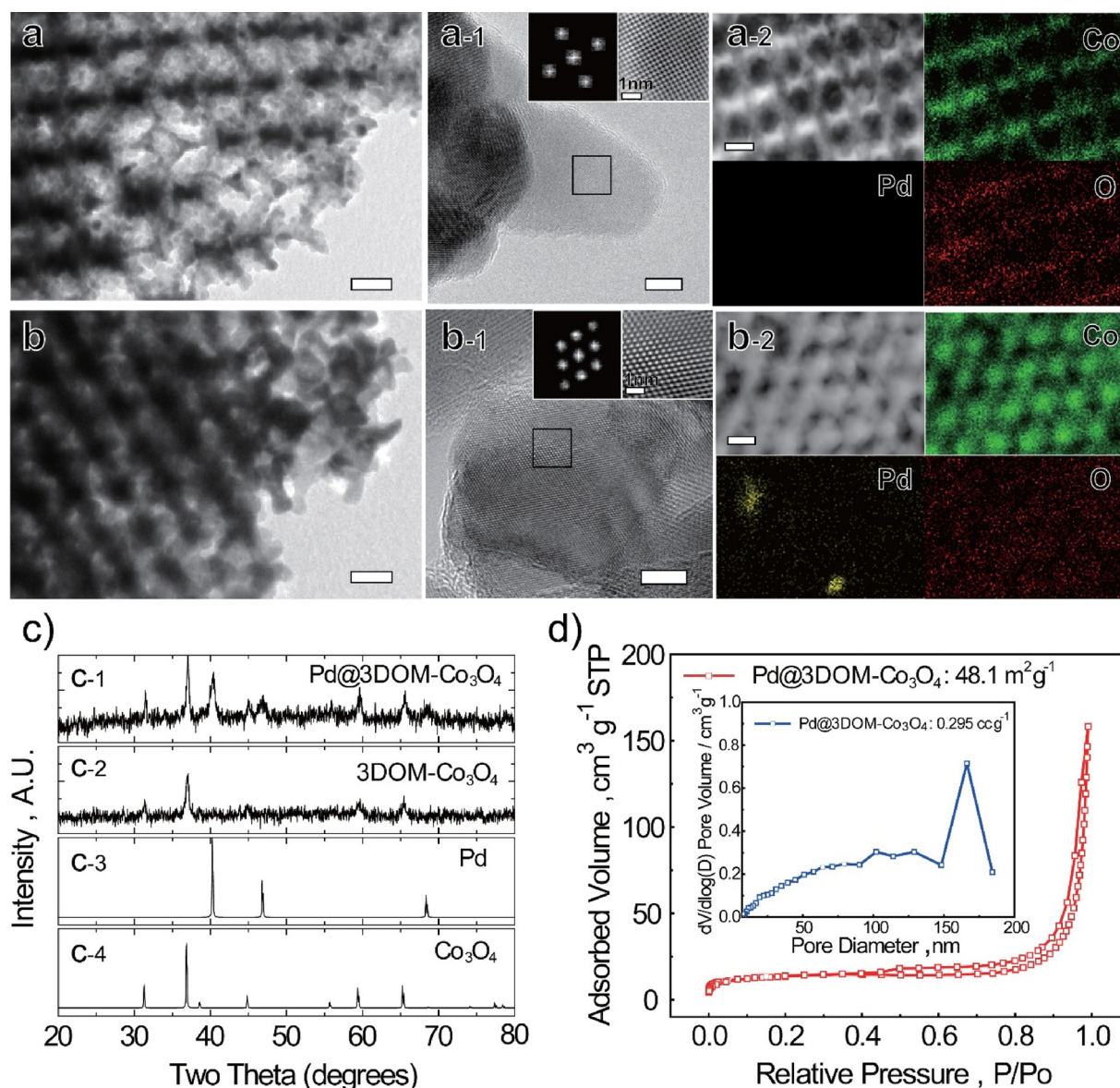


**Fig. 2.** Morphological and structural characterization of Pd@3DOM-Co<sub>3</sub>O<sub>4</sub>. a and b) HRTEM images of 3DOM-Co<sub>3</sub>O<sub>4</sub> and Pd@3DOM-Co<sub>3</sub>O<sub>4</sub>, respectively (Scale bar, 50 nm), with (a-1 and b-1) selected area electron diffraction (SAED) pattern (Scale bar, 5 nm) and (a-2 and b-2) element mapping images including cobalt (green), Pd (yellow), and oxygen (red) (Scale bar, 50 nm), c) X-ray diffraction (XRD) patterns of (c-1) Pd@3DOM-Co<sub>3</sub>O<sub>4</sub> and (c-2) 3DOM-Co<sub>3</sub>O<sub>4</sub> investigated in this study, and the bulk (c-3) Pd and (c-4) Co<sub>3</sub>O<sub>4</sub>, calculated XRD patterns based on ICSD, d) Nitrogen adsorption-desorption isotherm (Red) and pore size distribution (Blue) of Pd@3DOM-Co<sub>3</sub>O<sub>4</sub>. (For interpretation of the references to colour in this figure legend, the reader is referred to the web version of this article).

Co<sup>3+</sup> rich composition [60]. Our results support the latter work, since increased Co<sup>3+</sup> density in the Pd@3DOM-Co<sub>3</sub>O<sub>4</sub> revealed higher OER catalytic activity.

To investigate the electrocatalytic activities of Pd@3DOM-Co<sub>3</sub>O<sub>4</sub> toward both ORR ( $\text{O}_2 + 2\text{H}_2\text{O} + 4\text{e}^- \rightarrow 4\text{OH}^-$ ) and OER ( $4\text{OH}^- \rightarrow \text{O}_2 + 2\text{H}_2\text{O} + 4\text{e}^-$ ), rotating disk electrode (RDE) voltammetry was carried out in the half-cell condition [15,61]. The cyclic voltammetry (CV) of Pd@3DOM-Co<sub>3</sub>O<sub>4</sub>, 3DOM-Co<sub>3</sub>O<sub>4</sub>, Pt/C, Pd/C and Ir/C was conducted in N<sub>2</sub>-saturated 0.1 M KOH, with results shown in Fig. S1. ORR polarization curves shown in Fig. 4a and Fig. S2 demonstrated superior catalytic activity of Pd@3DOM-Co<sub>3</sub>O<sub>4</sub> towards ORR in comparison to 3DOM-Co<sub>3</sub>O<sub>4</sub> as well as Pt/C, Pd/C and Ir/C precious-metal benchmark catalysts, by evaluating the half-wave potential ( $E_{1/2}$ ), specific kinetic current ( $j_k$ ) normalized by geometric area, and ORR potential at the current density of  $-0.1 \text{ mA cm}^{-2}$  ( $E_{\text{ORR}}$ ) (refer to Table 1). Particularly, Pd@3DOM-Co<sub>3</sub>O<sub>4</sub> is observed to demonstrate comparable  $E_{1/2}$ ,  $E_{\text{ORR}}$ , and  $j_k$  (0.881 V, 0.986 V, and  $2.74 \text{ mA cm}^{-2}$  at

0.9 V vs. RHE, respectively) compared to those of state-of-the-art Pt/C (0.898 V, 1.00 V, and  $3.71 \text{ mA cm}^{-2}$  at 0.9 V vs. RHE, respectively) [62]. Meanwhile, the ORR curve of Pd/C exhibits a negatively shifted  $E_{1/2}$ ,  $E_{\text{ORR}}$ , and lower  $j_k$  (0.861 V, 0.981 V, and  $1.59 \text{ mA cm}^{-2}$  at 0.9 V vs. RHE, respectively) compared to those of Pt/C. Moreover, the number of electrons transferred ( $n$ ) during ORR on Pd@3DOM-Co<sub>3</sub>O<sub>4</sub> was obtained to investigate the electron pathway of the electrocatalytically active sites (Fig. S5). The K-L slope obtained by the Koutecky-Levich (K-L) plot corresponded to almost four electrons ( $n \approx 3.9$ ) transferred, demonstrating a pseudo-four electron pathway, which is further indicative of the excellent ORR kinetics of Pd@3DOM-Co<sub>3</sub>O<sub>4</sub>.

Besides the electrochemical ORR activity, OER activity of the catalysts were investigated by CV as shown in Fig. 4b and Fig. S3. Both Pd/C and Pt/C demonstrated poor OER activities with current density lower than  $13 \text{ mA cm}^{-2}$  at 2.0 V, which was expected due to their well-known insufficient bifunctionality towards both oxygen reactions. 3DOM-Co<sub>3</sub>O<sub>4</sub>, on the other hand, demonstrated significantly higher

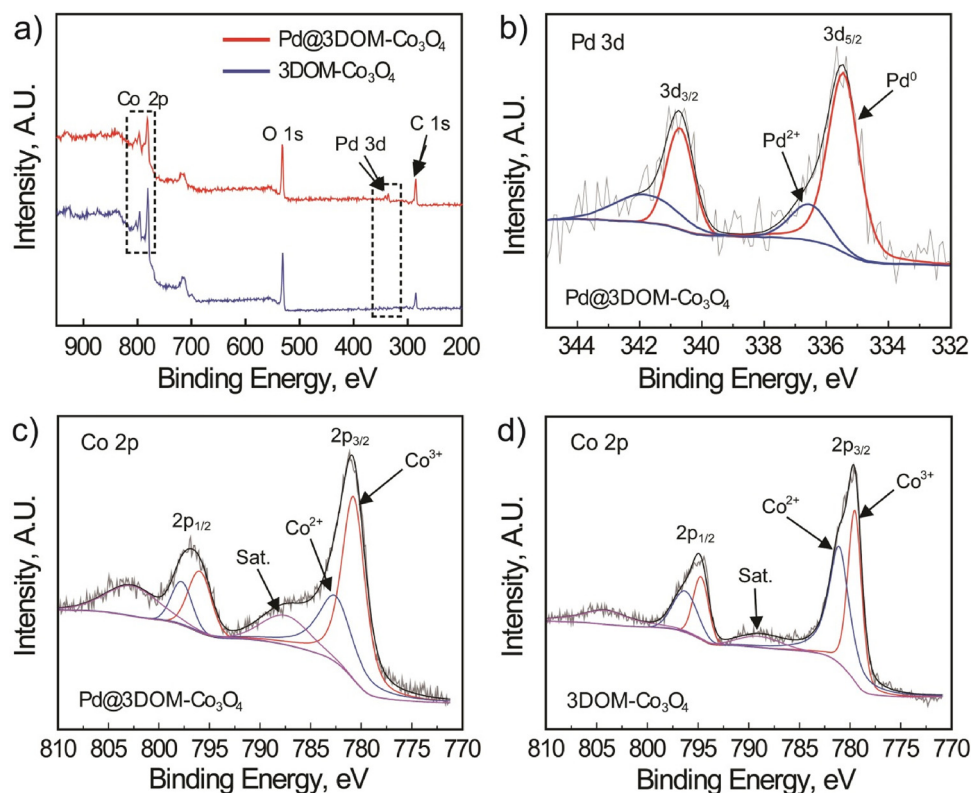


**Fig. 3.** Investigations on catalyst surface information of Pd@3DOM-Co<sub>3</sub>O<sub>4</sub> by X-ray photoelectron spectroscopy (XPS). a) full XPS survey scan of Pd@3DOM-Co<sub>3</sub>O<sub>4</sub> and 3DOM-Co<sub>3</sub>O<sub>4</sub> and deconvoluted Pd 3d (b) and Co 2p (c) peaks in Pd@3DOM-Co<sub>3</sub>O<sub>4</sub> and Co 2p (d) peak in 3DOM-Co<sub>3</sub>O<sub>4</sub>.

OER activity with a relatively lower overpotential of 0.41 V (1.64 V vs. RHE at 2.0 mA cm<sup>-2</sup>) and much higher current density of 34.8 mA cm<sup>-2</sup> at 2.0 V due to its structural advantages discussed above. Interestingly, Pd@3DOM-Co<sub>3</sub>O<sub>4</sub> demonstrated even higher current density of 41.3 mA cm<sup>-2</sup> at 2.0 V with a lower overpotential of 0.38 V relative to 3DOM-Co<sub>3</sub>O<sub>4</sub>. When compared to Ir/C (one of the best known OER benchmark noble catalysts), which demonstrated a very high  $E_{\text{OER}}$  (1.57 V vs. RHE) and current density at 2.0 V (40.6 mA cm<sup>-2</sup>), Pd@3DOM-Co<sub>3</sub>O<sub>4</sub> performed very similarly in terms of both  $E_{\text{OER}}$  and current density. The comprehensive electrochemical results are shown in Table 1. In brief, Pd@3DOM-Co<sub>3</sub>O<sub>4</sub> demonstrates enhanced bifunctional activities towards both ORR and OER, which is attributed to the synergy between chemically deposited-Pd and 3DOM-Co<sub>3</sub>O<sub>4</sub>. This will be further discussed and elucidated by *ab-initio* computational studies.

The DFT calculations provide insight into the electronic structure and corroborate the enhanced electrocatalytic activity of Pd@3DOM-Co<sub>3</sub>O<sub>4</sub>. Through modification of the electronic band structure by Pd-deposition, the electron abundance at the Fermi level is increased in the DOS of Co (Fig. S5) leading to higher electrical conductivity of Pd@3DOM-Co<sub>3</sub>O<sub>4</sub> than 3DOM-Co<sub>3</sub>O<sub>4</sub> alone. This indicates the chemical deposition of Pd helps Co<sub>3</sub>O<sub>4</sub> to have much improved electrical conductivity jumping over the poor nature of Co<sub>3</sub>O<sub>4</sub> itself and this triggers more rapid electron transfers during both oxygen reactions (ORR and OER), resulting in improved electrocatalytic activities. Regarding oxygen adsorption kinetics through d-band theory [32,35], Pd typically has a high-lying d-band center ( $\epsilon_d = -1.82$  eV) that increases oxygen binding energy, leading to slower kinetics for ORR [27,34,55]. The combination of deposited Pd with the 3DOM-Co<sub>3</sub>O<sub>4</sub> support, however, results in improved ORR performance of Pd@3DOM-Co<sub>3</sub>O<sub>4</sub>. This is attributed to the modified electronic structure of chemically deposited Pd, resulting in a low-lying d-band weight ( $\epsilon_d = -1.98$  eV, calculated as described in the experimental section) which designates weaker bonding with oxygen.

The degradation pathways of catalysts in electrochemical devices are

known to proceed by electrochemical dissolution of metals, oxide formation, agglomeration, and corrosion of support materials [40,41,63,64]. In metal-air batteries, high potentials incurred during charging pose harsh conditions for catalysts to retain their original electrochemical surface properties and electrocatalytic activities due to the extremely oxidative irreversible reactions [65]. To demonstrate and explain the excellent electrocatalytic durability of Pd@3DOM-Co<sub>3</sub>O<sub>4</sub>, direct electrochemical dissolutions of metal catalysts and corrosion of carbon supports were investigated through both experiment and *ab-initio* study (see the initial models of the catalysts surface in Fig. S4 and S6). Accelerated degradation testing (ADT) was conducted via repetitive CV (1000 cycles) in the OER potential region with a scan rate of 50 mV s<sup>-1</sup> to systematically evaluate the electrocatalytic stability of Pd@3DOM-Co<sub>3</sub>O<sub>4</sub> towards OER relative to the other catalysts. After 1000 repetitive OER cycles (only 100 cycles applied to Pd/C and Pt/C), the polarization curves and current densities obtained at 2.0 V vs. RHE for each catalyst are summarized in Fig. 4d and f, respectively, and in Table 1. The highest current retention (at 2.0 V vs. RHE) was observed with Pd@3DOM-Co<sub>3</sub>O<sub>4</sub> (96.4%) compared to 3DOM-Co<sub>3</sub>O<sub>4</sub> and benchmarks Pd/C and Ir/C (71.8%, 29.8%, and 30.8%, respectively). This highlights the extremely durable nature of Pd@3DOM-Co<sub>3</sub>O<sub>4</sub> towards the electrochemical oxidative conditions of OER typically occurring in the high overpotential range. Similarly for ORR, Pd@3DOM-Co<sub>3</sub>O<sub>4</sub> demonstrates negligible half-wave potential and specific kinetic current losses with very high retentions of 99.5% and 84.6%, respectively, compared to those of Pt/C (71.7% and 7.2%), and Pd/C (73.5% and 7.5%) as shown in Fig. 4c and e, which is in good agreement with the durability results in OER. 3DOM-Co<sub>3</sub>O<sub>4</sub> without Pd displays very low specific kinetic current densities at 0.9 V vs. RHE both before and after ADT due to the facts that it has virtually no electrochemical ORR activity at 0.9 V vs. RHE and the onset potential is more negative than 0.9 V, as demonstrated in Fig. 4a and c. Based on these electrochemical tests, superior ORR and OER activities and excellent electrochemical durability of Pd@3DOM-Co<sub>3</sub>O<sub>4</sub> were clearly observed, which will be further investigated by DFT computational analysis.

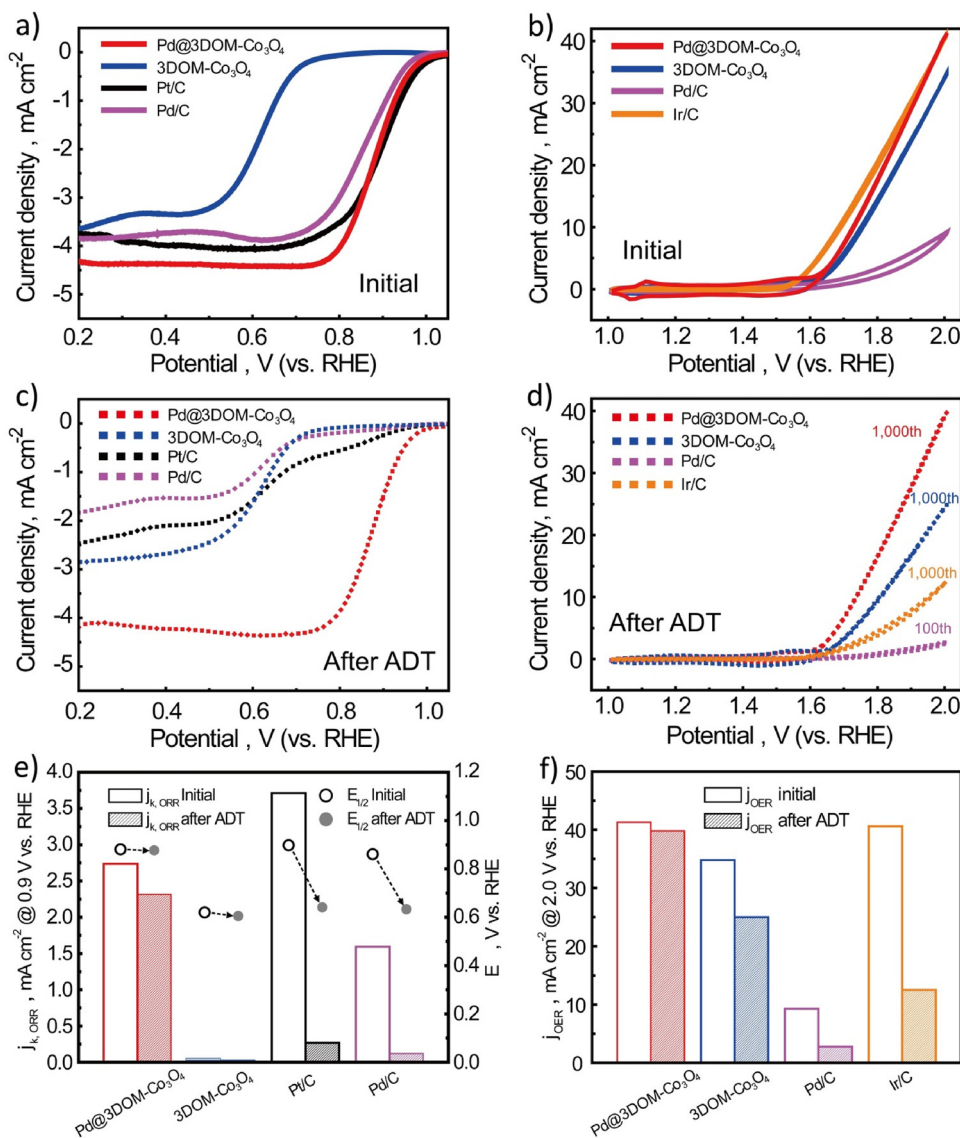
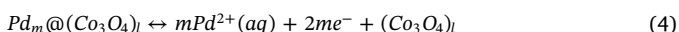
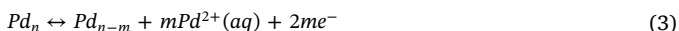


**Fig. 4.** Evaluation of oxygen reduction and evolution reaction (ORR and OER). a and b) initial ORR and OER polarization curves of Pd@3DOM-Co<sub>3</sub>O<sub>4</sub>, 3DOM-Co<sub>3</sub>O<sub>4</sub>, Pd/C, and Pt/C or Ir/C, respectively, and (c and d) final (after accelerated degradation testing (ADT)) ORR and OER polarization curves of Pd@3DOM-Co<sub>3</sub>O<sub>4</sub>, 3DOM-Co<sub>3</sub>O<sub>4</sub>, Pd/C, and Pt/C or Ir/C, respectively, (e) changes in specific kinetic current density and ORR half-wave potential of the electrocatalysts before and after ADT, (f) change in OER current density at 2.0 V vs. RHE of the electrocatalysts before and after ADT.

To understand the fundamental mechanisms behind the high electrochemical stability of Pd@3DOM-Co<sub>3</sub>O<sub>4</sub>, two basic chemical reactions were considered for employing *ab-initio* calculations as shown in the following equations (Eqs. (1) and (2)):



Pd<sub>13</sub> and Pd<sub>55</sub> nanoparticles (Fig. 5a) and slab models of Pd (111) (Fig. 5b), Co<sub>3</sub>O<sub>4</sub> (001) (Fig. 5c) and Pd monolayer deposited on Co<sub>3</sub>O<sub>4</sub> (001) (Fig. 5d) were designed to investigate the Pd dissolution potential ( $U_{diss,Pd}$ ) as a descriptor for thermodynamic stability. The  $U_{diss,Pd}$  considers the outermost M shell of the Pd nanoparticle and the Pd monolayer on Co<sub>3</sub>O<sub>4</sub>, as given by the following chemical equations (Eqs. (3) and (4)), respectively):



The standard Gibbs energy of reaction for dissolution of the Pd

particle and the Pd monolayer on Co<sub>3</sub>O<sub>4</sub> can be expressed as follows (Eqs. (5) and (6), respectively):

$$\Delta G^\circ = \mu^\circ(Pd_{n-m}) + m\{\mu^\circ(Pd^{2+}_{aq}) + kT \ln(a_{Pd^{2+}})\} - 2m(\mu^\circ_e - e\Delta U_{diss,Pd}) - \{\mu^\circ(Pd_{n,s}) + kT \ln(a_{Pd_n})\} \quad (5)$$

$$\Delta G^\circ = \mu^\circ(Pd_{n-m}) + m\{\mu^\circ(Pd^{2+}, aq) + kT \ln(a_{Pd^{2+}})\} - 2me(\mu^\circ_e - e\Delta U_{diss,Pd}) + \{\mu^\circ(\text{Co}_3\text{O}_4)_l + kT \ln(a_{(\text{Co}_3\text{O}_4)_l})\} - \{\mu^\circ(Pd_n@(\text{Co}_3\text{O}_4)_l) + kT \ln(a_{Pd_n@(\text{Co}_3\text{O}_4)_l})\} \quad (6)$$

where  $\mu^\circ$  is the standard chemical potential,  $k$  is the Boltzmann constant,  $a$  is the activity coefficient and  $T$  is the temperature. Then, the  $U_{diss,Pd}$  was derived based on the free energy via the following equations (Eqs. (7) and (8)):

$$U_{diss,Pd} = U_{bulk} + \frac{1}{2me}\{mE(Pd_{bulk}) + E(Pd_{n-m}) - E(Pd_n)\} \quad (7)$$

$$U_{diss,Pd} = U_{bulk} + \frac{1}{2ne}\{E(Pd_n) + E((\text{Co}_3\text{O}_4)_l) - E(Pd_n@(\text{Co}_3\text{O}_4)_l)\} \quad (8)$$



**Table 1**

Comparison of ORR and OER activity data before/after acceleration degradation testing (ADT) (1000 cycles in potential range from 1.0 V to 2.0 V vs. RHE among various catalysts.

Catalysts	ORR					
	$E_{\text{ORR}}^a$ @ $-0.1$ mA cm $^{-2}$ , V		$E_{1/2}^b$ , V		$j_k$ , mA cm $^{-2}$ @ 0.9 V	
	Before	After	Before	After	Before	After
	Before	After	Before	After	Before	After
Pd@3DOM-Co $_3$ O $_4$	0.986	0.978	0.881	0.877	2.737	2.316
3DOM-Co $_3$ O $_4$	0.733	0.723	0.620	0.605	–	–
Ir/C	0.881	0.784	0.772	0.637	–	–
Pd/C	0.981	0.785	0.861	0.633*	1.594	0.119
Pt/C	1.00	0.913	0.898	0.641*	3.713	0.269

Catalysts	OER				$\Delta E^d$ (= $E^c - E^a$ ), V	
	$E_{\text{OER}}^c$ @ 2 mA cm $^{-2}$ , V		$j$ @ 2 V vs. RHE, mA cm $^{-2}$		$\Delta E^d$ (= $E^c - E^a$ ), V	
	Before	After	Before	After	Before	After
	Before	After	Before	After	Before	After
Pd@3DOM-Co $_3$ O $_4$	1.611	1.666	41.3	39.8	0.625	0.683
3DOM-Co $_3$ O $_4$	1.641	1.672	34.8	25.0	0.908	0.949
Ir/C	1.573	1.728	40.6	12.5	0.692	0.944
Pd/C	1.725	1.961	9.27	2.76	0.744	1.176
Pt/C	1.675	2 <	12.2	1.72	0.675	2 <

$E_{\text{ORR}}^a$  =  $E_{\text{ORR}}$  defined at  $-0.1$  mA cm $^{-2}$ .

$E_{1/2}^b$  = Half-wave potential.

$E_{\text{OER}}^c$  =  $E_{\text{OER}}$  defined at 2 mA cm $^{-2}$ .

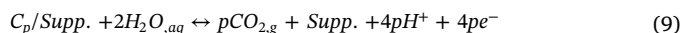
\* potentials of the catalysts were obtained only after 100 cycle in ADT.

The dissolution potentials of various forms of Pd are arranged in Fig. 5i. The reaction potentials shown in Fig. 5i are calculated based on the standard hydrogen electrode (SHE) to show all of the reactions that are relevant to the operation of a rechargeable zinc-air battery on a single potential scale. The calculated  $U_{\text{bulk}}$  of Pd slab model (bulk surface, Fig. 5b) of 0.81 V vs. SHE is found to be lower than  $U_{\text{diss}}$  of Pt (1.01 V vs. SHE). The  $U_{\text{diss}}$  of Pd $_{13}$  and Pd $_{55}$  nanoparticles (Fig. 5a) in DFT design are determined to be 0.16 and 0.49 V vs. SHE, respectively. The larger Pd $_{55}$  particle resulted in higher dissolution potential, indicating higher electrochemical stability as supported in previous reports [39,66]. In the Zn-air battery chemistry, the oxygen reduction potential at the air electrode is 0.4 V vs. SHE, which means the smaller sized Pd $_{13}$  nanoparticle with a diameter of 0.5 nm is thermodynamically unstable. Although the Pd $_{55}$  nanoparticle with a diameter of 1.1 nm maintains its solid phase with relatively higher thermodynamic stability within the potential range, it is likely to dissolve at potentials above 0.49 V vs. SHE during charging of the Zn-air battery ( $E^+ > 1.65$  V and  $E_{\text{(air electrode)}} > 0.4$  V). Interestingly, in contrast, the  $U_{\text{diss,Pd}}$  of Pd monolayer on Co $_3$ O $_4$  (Fig. 5d) is comparable to the  $U_{\text{diss,Pd}}$  of Pd bulk, which means the catalyst is likely to maintain its solid phase if the cathode potential of the battery can be maintained below 0.74 V vs. SHE. This computational prediction of a relatively high  $U_{\text{diss,Pd}}$  of Pd on 3DOM-Co $_3$ O $_4$  is consistent with the experimentally observed extreme durability of Pd@3DOM-Co $_3$ O $_4$  in the half-cell evaluation discussed earlier.

High surface area carbon materials are commonly used as catalyst supports to provide efficient pathways for electron transfer and facilitate reactant flux, as well as to disperse nano-sized catalyst particles that tend to agglomerate due to high surface energies [67]. Particularly for oxide materials such as Co $_3$ O $_4$  that have intrinsically lower electrical conductivity than metals, they are usually combined with carbon materials to effectively utilize their ORR/OER catalytic properties [17,18]. For rechargeable Zn-air battery testing conducted in this study, Pd@3DOM-Co $_3$ O $_4$  was dispersed on a microporous layer made of carbon GDL, which acts as a conductive and porous support. Therefore, it is

important to understand the electrochemical corrosion mechanism of the carbon support since it has direct influence on the cycle life of the battery. Accordingly, to simulate stability of the carbon material supporting various catalysts, a carbon monolayer (e.g. graphene) was designed on Pd (111), Ir(111), Co $_3$ O $_4$  (001), and Pd@Co $_3$ O $_4$  (001) as shown in Fig. 5e-h (initial models in Fig. S7).

The calculation of the equilibrium potential for carbon corrosion ( $U_{\text{corr,C}}$ ) starts with Eq. [9] shown below, which represents the reaction of carbon oxidation on the supported catalysts.



The  $U_{\text{corr,C}}$  on graphene can be obtained via calculating the change in the standard Gibbs free energy ( $\Delta G^\circ$ ) as described in Eq. (10) below.

$$\begin{aligned} \Delta G^\circ = & p(\mu_{CO_{2,g}}^\circ + kT \ln a_{CO_2}) + (\mu_{\text{Supp},s}^\circ + kT \ln a_{\text{Supp},s}) \\ & + 4p(\mu_{H^+,aq}^\circ + kT \ln a_{H^+}) + 4p(\mu_e^\circ - e\Delta U_{\text{corr,C}}) \\ & - (\mu_{C_p/\text{Supp},s}^\circ + kT \ln a_{C_p/\text{Supp},s}) - 2p(\mu_{H_2O,aq}^\circ + kT \ln a_{H_2O,aq}) \end{aligned} \quad (10)$$

Lastly, the  $U_{\text{corr,C}}$  was derived based on the free energy above Eq. (10) as presented in the following equation (Eq. (11));

$$\begin{aligned} U_{\text{corr,C}} = & \frac{1}{4pe} (E_{C_p/\text{Supp},s} + 2pE_{H_2O,aq} - pE_{CO_{2,g}} - E_{\text{Supp},s} - 2pE_{H_{2,g}} \\ & - 4p \times 0.059pH) \end{aligned} \quad (11)$$

where the support (Supp.) is Pd, Ir, Co $_3$ O $_4$  or Pd@Co $_3$ O $_4$  in each case. Graphite is oxidized at potentials over 0.207 V vs. RHE, which is the standard potential for the electrochemical oxidation of carbon in aqueous electrolyte [68]. The  $U_{\text{corr,C}}$  of a graphene monolayer was evaluated to be 0.196 V, which is slightly lower than graphite designed by DFT model as exhibited in Fig. S8. Interestingly,  $U_{\text{corr,C}}$  is significantly decreased when carbon is deposited on noble metals and metal oxides, with values of 0.065, 0.078 V, and  $-0.034$  V vs. SHE on Pd, Ir, and Co $_3$ O $_4$  surfaces, respectively. Pd/C has a very low electrochemical stability and demonstrated severe degradation during exposure to high OER potentials as shown in Fig. 4a-d (Pt/C shows a similar result in Fig. 4a and c, and S3), which is attributed to the fact that the dissolution of carbon accelerates the agglomeration and loss of Pt and Pd nanoparticles. Accordingly, their low  $U_{\text{corr,C}}$  likely led to the catalyst deactivation only after 100 OER cycles, resulting in significantly negative shifted  $E_{1/2}$  by 214 mV and 257 mV, respectively (refer to Table 1). Similarly, Ir/C shows severe degradation having  $E_{1/2}$  negatively shifted by 128 mV after ADT, although the degree of degradation is less than Pt and Pd. The degradation of Ir/C observed experimentally is most likely due to the dissolution of Ir as well as carbon corrosion. Meanwhile, despite the lower  $U_{\text{corr,C}}$ , 3DOM-Co $_3$ O $_4$  demonstrates much greater OER durability than carbon-supported noble metals in the experiment, which is due to its stability in alkaline media within the OER potential range [69]. In the case of Pd@3DOM-Co $_3$ O $_4$ , however, it is revealed that the  $U_{\text{corr,C}}$  of the carbon monolayer on Pd@3DOM-Co $_3$ O $_4$  is significantly increased with a value of 0.1 V vs. SHE, which predicts a much inhibited rate of carbon corrosion. This is consistent with the experimentally observed excellent stability of Pd@3DOM-Co $_3$ O $_4$ , having only slightly shifted to the final  $E_{\text{OER}}$  of 1.67 V after ADT from the initial performance of 1.61 V. More notably, as determined previously, the OER current retention of Pd@3DOM-Co $_3$ O $_4$  after 1000 OER cycles was 96.4%, whereas 3DOM-Co $_3$ O $_4$  itself and Ir/C only retained 71.8% and 30.8% of the initial activity, respectively.

In addition to half-cell testing, Pd@3DOM-Co $_3$ O $_4$  was tested as a bifunctional catalyst in an electrically rechargeable Zn-air battery prototype (Fig. S9). Fig. 6a shows the charge and discharge polarization curves of various electrocatalysts. Although the open circuit voltage (OCV) for Pd@3DOM-Co $_3$ O $_4$  (1.43 V) is slightly lower than that for Pt/C (1.46 V), the discharge potential is highly competitive to that of Pt/C particularly at higher current densities. In contrast, 3DOM-Co $_3$ O $_4$  and



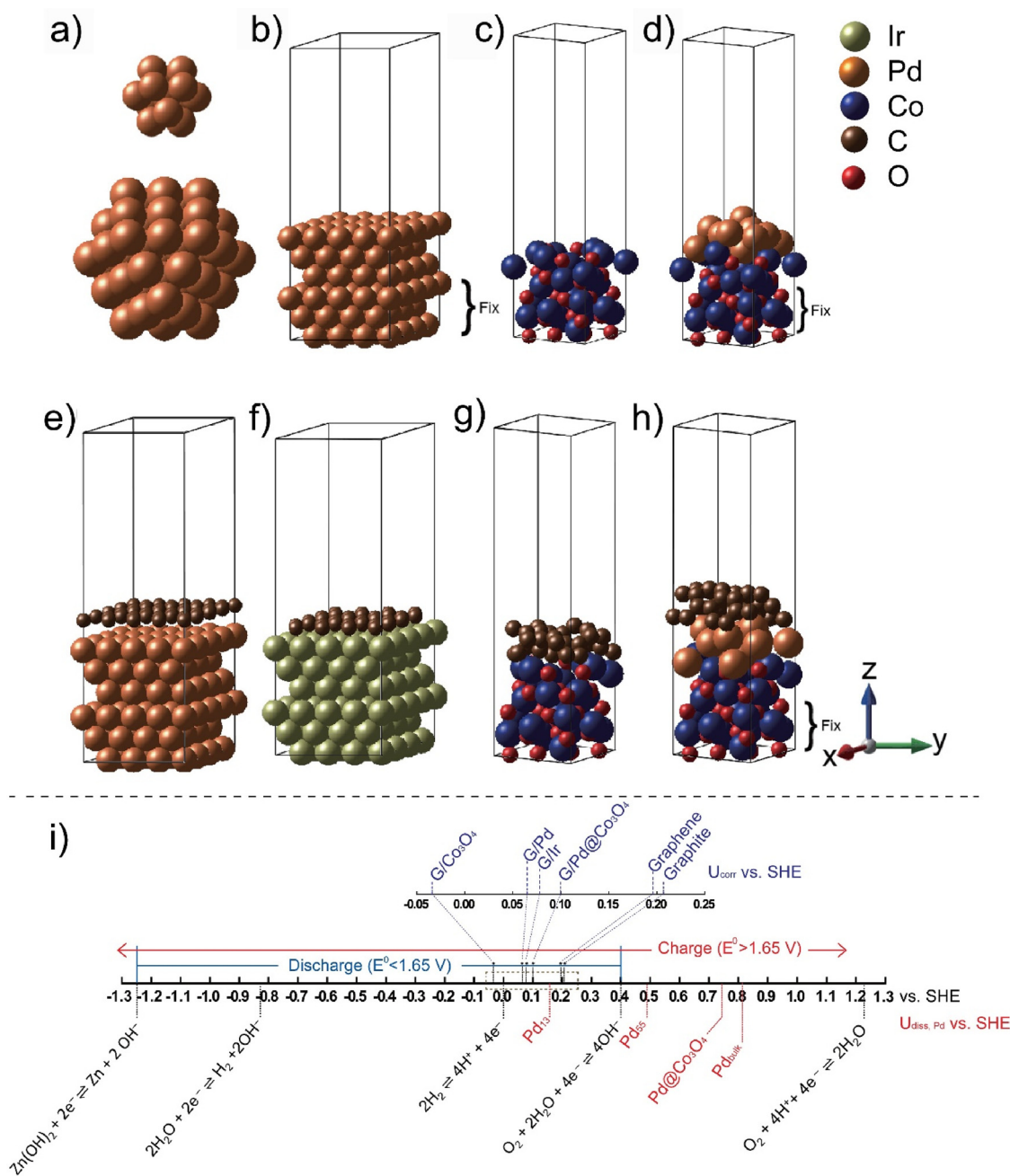


**Fig. 5.** Considered DFT models, and schematic equilibrium potentials in Zn-air cell denoting the  $U_{\text{diss, Pd}}$  and  $U_{\text{corr, C}}$  of Pd and carbon. a) Relaxed  $\text{Pd}_{13}$  and  $\text{Pd}_{55}$  nanoparticles, and slab models of (b) Pd (111) (c)  $\text{Co}_3\text{O}_4$  (001) and (d) Pd monolayer deposited on  $\text{Co}_3\text{O}_4$  (001), and the designed models of graphene deposited on (e) Pd, (f) Ir, (g)  $\text{Co}_3\text{O}_4$  (001) and (h)  $\text{Pd@Co}_3\text{O}_4$  (001) after structural relaxation. (i) Potential window illustrating relevant electrochemical reactions and dissolution potentials of carbon and Pd.

Ir/C demonstrate relatively lower discharge potentials and greater loss of activity at high current densities, resulting in larger overpotentials and lower efficiency. During charging,  $\text{Pd@3DOM-Co}_3\text{O}_4$  shows comparable charge potential to that of Ir/C, while the overpotential of  $\text{Pd@3DOM-Co}_3\text{O}_4$  is much lower than that of Ir/C in the low current density region. Taken together,  $\text{Pd@3DOM-Co}_3\text{O}_4$  demonstrates enhanced bi-functional electrocatalytic activity with the least overpotential over the large range of applied charge and discharge current densities, which is consistent with the trends observed from both ORR and OER half-cell evaluations (Table 1). As shown in Fig. 6b, the electrically rechargeable Zn-air battery with  $\text{Pd@3DOM-Co}_3\text{O}_4$  exhibits great rechargeability as well as synergistically improved activity, where the catalyst demonstrates far lower initial overpotential ( $0.84\text{ V}$  at  $10\text{ mA cm}^{-2}$ ) between

discharge and charge potentials than those with Pt/C ( $0.89\text{ V}$ ), Ir/C ( $0.86\text{ V}$ ) and  $\text{Co}_3\text{O}_4$  ( $1.0\text{ V}$ ). The battery reliably operated for 300 charge/discharge cycles over a period of 50 h (10 min per a charge/discharge cycle) while effectively retaining its initial performance, which is significantly greater than  $3\text{DOM-Co}_3\text{O}_4$  (210 cycles), Pt/C (6 cycles), and Ir/C (170 cycles). Moreover, a more extensive cycling test was conducted with one charge/discharge cycle lasting 10 h to explore the long term durability of  $\text{Pd@3DOM-Co}_3\text{O}_4$ , with results shown in Fig. 6c. As expected,  $\text{Pd@3DOM-Co}_3\text{O}_4$  demonstrated not only the least overpotential ( $0.66\text{ V}$  at  $1\text{ mA cm}^{-2}$ ), but also the longest cycle life without severe performance loss over 500 h, indicating its enhancements in terms of both electrocatalytic activity and stability.  $3\text{DOM-Co}_3\text{O}_4$  itself showed a moderate cycle life, with considerable

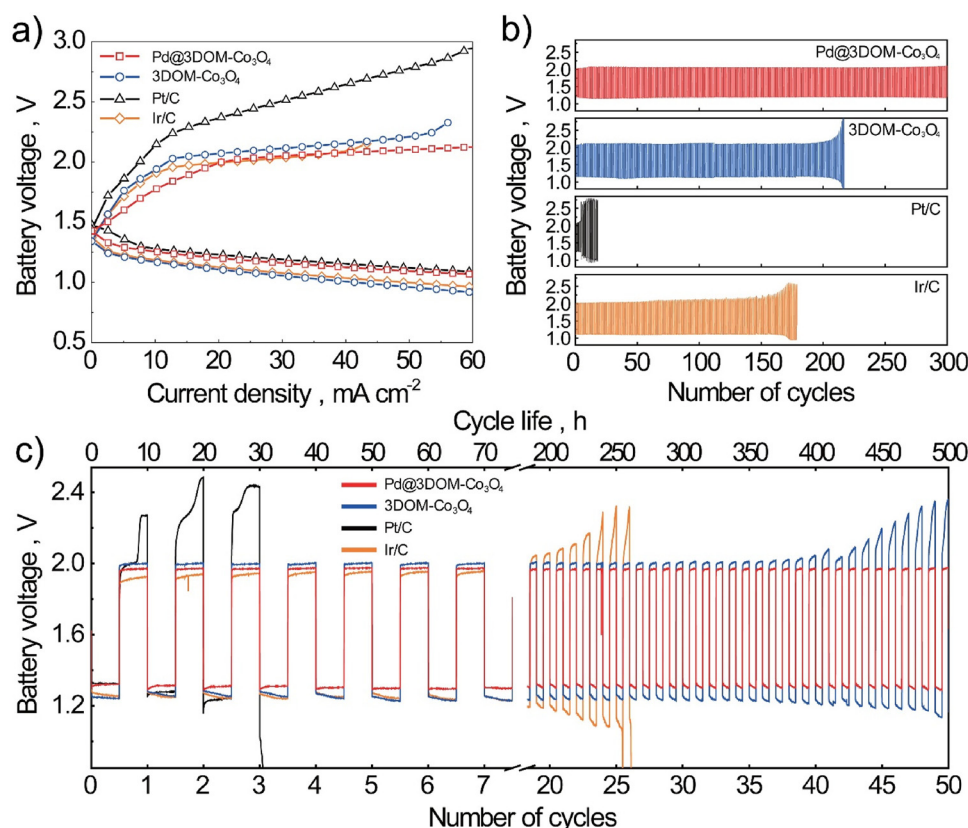


**Fig. 6.** Rechargeable Zn-air batteries with Pd@3DOM-Co<sub>3</sub>O<sub>4</sub> catalyst at the air electrode. a) Charge and discharge (C/D) polarization curves of the rechargeable Zn-air battery obtained at applied current densities; (b) C/D cycling performance of the rechargeable Zn-air battery using Pd@3DOM-Co<sub>3</sub>O<sub>4</sub>, 3DOM-Co<sub>3</sub>O<sub>4</sub>, Pt/C and Ir/C obtained with a 10 min cycle period and applied current density of 10 mA cm<sup>-2</sup>. (c) Long term C/D cycling performance of the electrocatalysts obtained with 10 h cycle period at 1 mA cm<sup>-2</sup>. The DC profile experiments were terminated above 2.5 V or below 0.5 V.

performance loss starting at the 40<sup>th</sup> cycle and drastically increased overpotentials thereafter, resulting in significant degradation of charge and discharge performances. Meanwhile, the precious-metal benchmark catalyst Pt/C lost its stable discharge and charge activities within the first cycle, indicating its instability in the high potential range during the charge process of the battery, whereas the performance of Ir/C degraded relatively slowly, terminating after 26 cycles of battery operation. The excellent rechargeability and extended cycle life observed with Pd@3DOM-Co<sub>3</sub>O<sub>4</sub> are most likely due to three main improvements: (i) a decrease in the d-band center of Pd (-1.98 eV) and the enhanced electron abundance at the Fermi level achieved by chemical deposition of Pd, which promotes increased kinetics of oxygen reactions and facilitates faster charge transfer, respectively, resulting in improved electrocatalytic activity and electrical conductivity, (ii) relatively higher carbon corrosion potential for Pd@3DOM-Co<sub>3</sub>O<sub>4</sub> ( $U_{\text{corr,C}} = 0.1$  V vs. SHE), resulting in less corroded surfaces and (iii) the increase in dissolution potential of Pd deposits within Pd@3DOM-Co<sub>3</sub>O<sub>4</sub> ( $U_{\text{diss,Pd}} = 0.74$  V vs. SHE), leading to both a thermodynamically and electrochemically stable catalyst even at high charging potentials within the Zn-air battery.

#### 4. Conclusions

The bifunctional ORR and OER activities and electrochemical stability observed with a unique three-dimensionally ordered mesoporous Pd@3DOM-Co<sub>3</sub>O<sub>4</sub> catalyst were elucidated by electrochemical testing and *ab-initio* computational calculation (DFT). Experimentally, both ORR and OER activities were observed to benefit from synergistically combining chemically deposited Pd and 3DOM-Co<sub>3</sub>O<sub>4</sub>, resulting in activities greater than those of the individual components. Specifically, Pd@3DOM-Co<sub>3</sub>O<sub>4</sub> showed a comparable half-wave potential ( $E_{1/2}$ ) of 0.881 V to that of the precious metal benchmark Pt/C (0.898 V) during ORR and significantly higher current density (41.3 mA cm<sup>-2</sup> at 2.0 V vs. RHE) and lower overpotential (0.38 V) compared to the precious

metal benchmark Ir/C (40.6 mA cm<sup>-2</sup> and 0.34 V) during OER. Both computational and physicochemical investigations were utilized to elucidate high bifunctional activities demonstrated by Pd@3DOM-Co<sub>3</sub>O<sub>4</sub>. Not only did the modified electronic structure of Pd on 3DOM-Co<sub>3</sub>O<sub>4</sub> result in a downward shift in  $\epsilon_d$  of Pd that weakens the bond with oxygen, resulting in increased ORR kinetics, but it also increased Co<sup>3+</sup> active sites in Co<sub>3</sub>O<sub>4</sub> after Pd deposition leading to improvements in the OER activity. Additionally, electron abundance at the Fermi level in the DOS of Co in Pd@3DOM-Co<sub>3</sub>O<sub>4</sub> enhances its electrical conductivity, promoting a rapid charge transfer during both oxygen reactions. Besides the enhanced bifunctional oxygen electrocatalysis, Pd@3DOM-Co<sub>3</sub>O<sub>4</sub> shows remarkable electrochemical stability in the severely oxidative potential range of OER. After 1000 cycles of accelerated degradation testing, Pd@3DOM-Co<sub>3</sub>O<sub>4</sub> demonstrated very high retentions of 99.5% and 84.6% of its initial half-wave potential and specific kinetic current, respectively, compared to those of Pt/C (71.7% and 7.2%) and Pd/C (73.5% and 7.5%). Moreover, while 3DOM-Co<sub>3</sub>O<sub>4</sub> without Pd and Ir/C showed high losses in their OER activity displaying 71.8% and 30.8% OER current retention, respectively, excellent OER stability was observed with Pd@3DOM-Co<sub>3</sub>O<sub>4</sub> showing 96.4% OER current retention. The superior experimentally-observed electrochemical durability was corroborated by DFT computational investigations of the bulk-like dissolution potential of Pd on 3DOM-Co<sub>3</sub>O<sub>4</sub> and the high corrosion potential of carbon on Pd@3DOM-Co<sub>3</sub>O<sub>4</sub>. The remarkable electrochemical activities and stabilities of Pd@3DOM-Co<sub>3</sub>O<sub>4</sub> resulted in excellent rechargeability of a prototype Zn-air battery, which demonstrates the attractiveness of the computationally-aided catalyst design demonstrated in this work.

#### Acknowledgements

M.H.S. and M.G.P. contributed equally to this work. The authors wish to acknowledge the support provided by the Natural Sciences and Engineering Research Council of Canada (NSERC) and by the University

of Waterloo and the Waterloo Institute for Nanotechnology. It was also supported by the Basic Science Research Program through the NRF and the New & Renewable Energy Core Technology Program of the KETEP [NRF-2017R1D1A1B04031539 & KETEP- 20173010032080]; and by development program of KIER [B8-2423] in Republic of Korea.

## Appendix A. Supplementary data

Supplementary material related to this article can be found, in the online version, at doi:<https://doi.org/10.1016/j.apcatb.2018.06.006>.

## References

- [1] B. Dunn, H. Kamath, J.M. Tarascon, *Science* 334 (2011) 928–935.
- [2] M.E. Scofield, H. Liu, S.S. Wong, *Chem. Soc. Rev.* 44 (2015) 5836.
- [3] Z.-L. Wang, D. Xu, J.-J. Xu, X.-B. Zhang, *Chem. Soc. Rev.* 43 (2014) 7746–7786.
- [4] D. Larcher, J.-M. Tarascon, *Nat. Chem.* 7 (2015) 19–29.
- [5] Y. Li, H. Dai, *Chem. Soc. Rev.* 43 (2014) 5257–5275.
- [6] J. Fu, Z.P. Cano, M.G. Park, A. Yu, M. Fowler, Z. Chen, *Adv. Mater.* (2017) 29.
- [7] D.U. Lee, P. Xu, Z.P. Cano, A.G. Kashkooli, M.G. Park, Z. Chen, *J. Mater. Chem. A* 4 (2016) 7107–7134.
- [8] F.F. Cheng, J. Shen, B. Peng, Y. Pan, Z. Tao, J. Chen, *Nat. Chem.* 3 (2011) 79–84.
- [9] M.P. Browne, H. Nolan, G.S. Duesberg, P.E. Colavita, M.E.G. Lyons, *ACS Catal.* 6 (2016) 2408–2415.
- [10] Q. Liu, Y. Wang, L. Dai, J. Yao, *Adv. Mater.* 29 (2016) 3000–3006.
- [11] J. Duan, S. Chen, M. Jaroniec, S.Z. Qiao, *ACS Catal.* 5 (2015) 5207–5234.
- [12] J. Zhang, Z. Zhao, Z. Xia, L. Dai, *Nat. Nanotech.* 10 (2015) 444–452.
- [13] D.U. Lee, H.W. Park, M.G. Park, V. Ismayilov, Z. Chen, *ACS Appl. Mater. Interfaces* 7 (2014) 902–910.
- [14] P. Ganesan, M. Prabu, J. Sanetuntikul, S. Shanmugam, *ACS Catal.* 5 (2015) 3625–3637.
- [15] H.W. Park, D.U. Lee, P. Zamani, M.H. Seo, L.F. Nazar, Z. Chen, *Nano Energy* 10 (2014) 192–200.
- [16] L. Li, S.-H. Chai, S. Dai, A. Manthiram, *Energ. Environ. Sci.* 7 (2014) 2630–2636.
- [17] M.H. Seo, H.W. Park, D.U. Lee, M.G. Park, Z. Chen, *ACS Catal.* 5 (2015) 4337–4344.
- [18] M.G. Park, D.U. Lee, M.H. Seo, Z.P. Cano, Z. Chen, *Small* 12 (2016) 2707–2714.
- [19] P. Hohenberg, W. Kohn, *Phys. Rev.* 136 (1964) B864–B871.
- [20] W. Kohn, L.J. Sham, *Phys. Rev. A* 140 (1965) A1133–A1138.
- [21] L. Li, S. Liu, A. Manthiram, *Nano Energy* 12 (2015) 852–860.
- [22] D.U. Lee, M.G. Park, H.W. Park, M.H. Seo, X. Wang, Z. Chen, *ChemSusChem* 8 (2015) 3129–3138.
- [23] B.Y. Xia, Y. Yan, N. Li, H.B. Wu, X.W. Lou, X. Wang, *Nat. Energy* 1 (2016) 15006.
- [24] A. Muthukrishnan, Y. Nabaie, T. Okajima, T. Ohsaka, *ACS Catal.* 5 (2015) 5194–5202.
- [25] J. Wang, K. Li, H.X. Zhong, D. Xu, Z.L. Wang, Z. Jiang, Z.J. Wu, X.B. Zhang, *Angew. Chem. Int. Ed.* 54 (2015) 10530–10534.
- [26] U.I. Kramm, I. Herrmann-Geppert, J. Behrends, K. Lips, S. Fiechter, P. Bogdanoff, *J. Am. Chem. Soc.* 138 (2016) 635–640.
- [27] J. Greeley, I.E.L. Stephens, A.S. Bondarenko, T.P. Johansson, H.A. Hansen, T.F. Jaramillo, J. Rossmeisl, I. Chorkendorff, J.K. Nørskov, *Nat. Chem.* 1 (2009) 552–556.
- [28] V.R. Stamenkovic, B. Fowler, B.S. Mun, G. Wang, P.N. Ross, C.A. Lucas, N.M. Markovic, *Science* 315 (2007) 493–497.
- [29] B. Hammer, J.K. Nørskov, *Nature* 376 (1995) 238–240.
- [30] B. Hammer, J.K. Nørskov, *Surf. Sci.* 343 (1995) 211–220.
- [31] U.B. Demirci, *J. Power Sources* 173 (2007) 11–18.
- [32] M. Shao, K. Sasaki, N.S. Marinkovic, L. Zhang, R.R. Adzic, *Electrochem. Commun.* 9 (2007) 2848–2853.
- [33] M.H. Shao, T. Huang, P. Liu, J. Zhang, K. Sasaki, M.B. Vukmirovic, R.R. Adzic, *Langmuir* 22 (2006) 10409–10415.
- [34] J. Greeley, M. Mavrikakis, *Nat. Mater.* 3 (2004) 810–815.
- [35] M.H. Shao, P. Liu, J. Zhang, R.R. Adzic, *J. Phys. Chem. B* 111 (2007) 6772–6775.
- [36] N. Ramaswamy, U. Tylus, Q. Jia, S. Mukerjee, *J. Am. Chem. Soc.* 135 (2013) 15443–15449.
- [37] J.E. Huheey, E.A. Keiter, R.L. Keiter, *Inorganic Chemistry: Principles of Structure and Reactivity*, 4<sup>th</sup> edition, (1993).
- [38] F. Calle-Vallejo, O.A. Díaz-Morales, M.J. Kolb, M.T.M. Koper, *ACS Catal.* 5 (2015) 869–873.
- [39] J.K. Seo, A. Khetan, M.H. Seo, H. Kim, B. Han, *J. Power Sources* 238 (2013) 137–143.
- [40] M.H. Seo, S.M. Choi, E.J. Lim, I.H. Kwon, J.K. Seo, S.H. Noh, W.B. Kim, B. Han, *Chemsuschem* 7 (2014) 2609–2620.
- [41] D. Higgins, M.A. Hoque, M.H. Seo, R. Wang, F. Hassan, J.-Y. Choi, M. Pritzker, A. Yu, J. Zhang, Z. Chen, *Adv. Funct. Mater.* 24 (2014) 4325–4336.
- [42] S.H. Noh, M.H. Seo, J.K. Seo, P. Fischer, B. Han, *Nanoscale* 5 (2013) 8625–8633.
- [43] G. Kresse, J. Furthmüller, *Phys. Rev. B* 54 (1996) 11169.
- [44] J.P. Perdew, K. Burke, M. Ernzerhof, *Phys. Rev. Lett.* 77 (1996) 3865.
- [45] G. Kresse, J. Furthmüller, *Comput. Mater. Sci.* 6 (1996) 15–50.
- [46] G. Kresse, D. Joubert, *Phys. Rev. B* 59 (1999) 1758.
- [47] P.E. Blöchl, *Phys. Rev. B* 50 (1994) 17953.
- [48] G. Hautier, S.P. Ong, A. Jain, C.J. Moore, G. Ceder, *Phys. Rev. B* 85 (2012) 155208.
- [49] C. Franchini, R. Podloucky, J. Paier, M. Marsman, G. Kresse, *Phys. Rev. B* 75 (2007) 195128.
- [50] Y.L. Lee, J. Kleis, J. Rossmeisl, D. Morgan, *Phys. Rev. B* 80 (2009) 224101.
- [51] M. Methfessel, A.T. Paxton, *Phys. Rev. B* 40 (1989) 3616–3621.
- [52] P.E. Blöchl, O. Jepsen, O.K. Andersen, *Phys. Rev. B* 49 (1994) 16223–16233.
- [53] P. Kratzer, B. Hammer, J.K. Nørskov, *J. Chem. Phys.* 105 (1996) 5595–6005.
- [54] M. Wakasaka, S. Mitsui, Y. Hirose, K. Kawashima, H. Uchida, M. Watanabe, *J. Phys. Chem. B* 110 (2006) 23489–23496.
- [55] M.H. Seo, S.M. Choi, D.U. Lee, W.B. Kim, Z. Chen, *J. Power Sources* 300 (2015) 1–9.
- [56] D. Su, S. Dou, G. Wang, *Sci. Rep.* 4 (2014) 5767.
- [57] H.Y. Wang, S.F. Hung, H.Y. Chen, T.S. Chan, H.M. Chen, B. Liu, *J. Am. Chem. Soc.* 138 (2016) 36–39.
- [58] P.W. Menezes, A. Indra, A. Bergmann, P. Chernev, C. Walter, H. Dau, P. Strasser, M. Driess, *J. Mater. Chem. A* 4 (2016) 10014–10022.
- [59] Y. Liang, H. Wang, J. Zhou, Y. Li, J. Wang, T. Regier, H. Dai, *J. Am. Chem. Soc.* 134 (2012) 3517–3523.
- [60] S. Li, S. Peng, L. Huang, X. Cui, A.M. Al-Enizi, G. Zheng, *ACS Appl. Mater. Interfaces* 8 (2016) 20534–20539.
- [61] H.W. Park, D.U. Lee, M.G. Park, R. Ahmed, M.H. Seo, L.F. Nazar, Z. Chen, *ChemSusChem* 8 (2015) 1058–1065.
- [62] B. Lim, M. Jiang, P.H.C. Camargo, E.C. Cho, J. Tao, X. Lu, Y. Zhu, Y. Xia, *Science* 324 (2009) 1302–1305.
- [63] S. Zhang, X. Yuan, H. Wang, W. Me'rida, H. Zhuc, J. Shen, S. Wu, J. Zhang, *Int. J. Hydrog. Energy* 34 (2009) 388–404.
- [64] Z.L. Wang, D. Xu, J.J. Xu, X.B. Zhang, *Chem. Soc. Rev.* 43 (2014) 7746–7786.
- [65] F. Cheng, J. Chen, *Chem. Soc. Rev.* 41 (2012) 2172–2192.
- [66] L. Tang, B. Han, K. Persson, C. Friessen, T. He, K. Sieradzki, G. Ceder, *J. Am. Chem. Soc.* 132 (2010) 596–600.
- [67] X.J. Zhou, J.L. Qiao, L. Yang, J.J. Zhang, *Adv. Energy Mater.* 4 (2014) 1301523.
- [68] D.R. Lide, *CRC Handbook of Chemistry and Physics*, 86th edition, (2005).
- [69] M. Pourbaix, *Atlas of Electrochemical Equilibria in Aqueous Solutions*, (1974).